

Can milliQan?

A search for millicharged particles at the Large Hadron Collider

Christina Dorofeev*
Department of Physics, University of Oregon

David Stuart,[†] Sai Neha Santpur,[‡] and Ryan Schmitz[§]
Department of Physics, University of California, Santa Barbara

(Dated: August 1, 2024)

We examine data from the milliQan experiment, which aims to detect millicharged particles (mCPs) predicted by extensions to the Standard Model (SM). Millicharged particles (χ), with charges much smaller than the elementary charge ($\epsilon \ll 1$), have been a subject of theoretical interest due to their potential implications for charge quantization. In addition to their role in grand unification theories, millicharged particles have been proposed in various hidden (dark) sector models introducing a new $U'(1)$ gauge symmetry. These models suggest that millicharged particles could interact through kinetic mixing with SM photons, offering a potential method for their detection. This paper provides an overview of the milliQan bar detector’s performance and alignment using muons produced in pp collisions at the Large Hadron Collider (LHC), focusing on the energy deposition, timing, flux, and trajectory of beam muons as they pass through the detector. This paper also analyzes the signal phase space by investigating sub-single photoelectron (sub-SPE) behavior in photomultiplier tubes (PMTs) and characterizing this background.

I. INTRODUCTION

The Standard Model (SM) of particle physics represents one of the most profound achievements in modern science [1]. Among its most remarkable successes is the prediction of the electron magnetic moment, with recent measurements reaching extraordinary precision that aligns with the Standard Model’s predictions to one part in one trillion [2]. While Standard Model predictions are largely supported by experimental observations, numerous questions remain unresolved [3, 4].

One of the most significant unresolved questions is the nature of dark matter. Gravitational observations have provided compelling evidence for the existence of dark matter, a form of matter that neither emits nor absorbs photons [5]. The spatial distribution of this dark matter is notably different from that of luminous matter, suggesting that the majority of the universe’s mass is governed by physical laws that extend beyond the framework of our current theories. While dark matter is known to interact gravitationally, this interaction alone does not reveal its fundamental nature. Various models have proposed single-particle candidates for dark matter, such as Weakly Interacting Massive Particles (WIMPs) and axions, and extensive searches have been conducted to detect them. Despite these efforts, no definitive evidence has been found, and many of the previously considered parameter spaces for these candidates have been excluded by experimental results [6, 7]. The

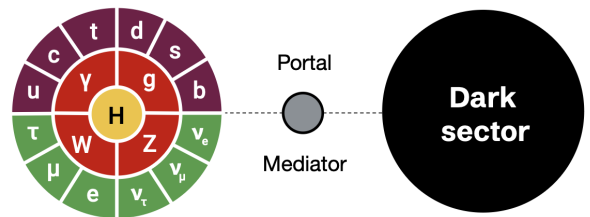


FIG. 1: Diagram showing the interaction between the Standard Model and the dark sector via a portal, which mediates non-gravitational interaction(s). An overview of dark sectors and dark-sector mediators is presented in Ref. [9].

WIMP and axion hypotheses remain well-motivated and continued searches are warranted [8]. Nevertheless, the exploration of new models could prove essential in addressing this profound question in physics.

Other Beyond Standard Model (BSM) theories propose that dark matter could consist of multiple particles, each interacting through mechanisms analogous to known forces. Recently, significant effort has been dedicated to studying BSM theories featuring a dark sector that interacts with the Standard Model through portal mechanisms as seen in Figure 1 [9, 10].

The dark sector could also provide answers to other fundamental questions, such as charge quantization, potentially addressed by fractionally charged particles arising in models introducing a new $U'(1)$ gauge symmetry [11]. Interestingly, the Standard Model does not provide an explanation for the quantization of

* christina.dorofeev@cern.ch

† davidstuart@ucsb.edu

‡ ssantpur@ucsb.edu

§ schmitz@ucsb.edu

electric charge. With no definitive evidence for grand unification or magnetic monopoles, the quantization of charge remains an unresolved mystery [12]. Since neither of these theories has yielded conclusive results, there are strong motivations to look for particles with charges lower than the electron charge.

A. Millicharged Particles

Fractionally charged particles are a known feature of the Standard Model, with all observed particles possessing electric charges that are integer multiples of $e/3$. However, some theoretical models introduce the possibility of particles with significantly smaller charges ($\mathcal{O}(10^{-3})$), referred to as millicharged particles (mCPs).

Millicharged particles can be appended to the Standard Model through several mechanisms. One possibility is the presence of an additional abelian gauge field that interacts with a massive dark fermion and mixes with SM hypercharge via a kinetic term. Holdom's work [11] presents a new $U'(1)$ symmetry group, introducing gauge bosons and fermions into the Dark Sector.

This method connects the Standard Model with the dark sector through the kinetic mixing term.

$$\mathcal{L} = \mathcal{L}_{\text{SM}} + \mathcal{L}_{\text{DS}} - \frac{\kappa}{2} A'_{\mu\nu} B^{\mu\nu} \quad (1)$$

where \mathcal{L}_{SM} and \mathcal{L}_{DS} represent the Lagrangians for the Standard Model and the dark sector, respectively. The terms $A'_{\mu\nu}$ and $B^{\mu\nu}$ denote the field strengths of the dark sector's Abelian vector field and the Standard Model's hypercharge field, respectively. The kinetic mixing between A' and B is defined by the mixing parameter κ . The physical consequences of the kinetic mixing operator depend on whether the dark vector field is massive or massless.

Adding the new $U'(1)$ group to the SM Lagrangian introduces a massless dark-photon (A') and massive dark-fermion (ψ)

$$\mathcal{L} = \mathcal{L}_{\text{SM}} - \frac{1}{4} A'_{\mu\nu} A'^{\mu\nu} + i\bar{\psi} (\not{\partial} + ie' A' + iM_{m\text{CP}}) \psi - \frac{\kappa}{2} A'_{\mu\nu} B^{\mu\nu} \quad (2)$$

The dark fermion carries a dark charge e' and has a mass $M_{m\text{CP}}$. The dark charge e' is of the same magnitude as the electron charge e due to the imposed symmetry. Redefining the gauge boson

$$A'_\mu \longrightarrow A'_\mu + \kappa B_\mu \quad (3)$$

leads to the dark fermion having a small electric charge ($\kappa e'$)

$$\mathcal{L} = \mathcal{L}_{\text{SM}} - \frac{1}{4} A'_{\mu\nu} A'^{\mu\nu} + i\bar{\psi} (\not{\partial} + ie' A' - i\kappa e' B + iM_{m\text{CP}}) \psi \quad (4)$$

The dark photon can interact with ordinary photons via kinetic mixing, enabling it to weakly couple with electrically charged particles. The mixing parameter κ , as shown in Equation 4, acts to suppress the strength of the interaction between the SM and dark sector. Hence, these dark fermions would appear to have an electric charge on the order of $10^{-3} e$.

Multiple searches have been conducted for millicharged particles, leading to several constraints on the possible values of their charge and mass [13–20]. mCPs can be pair-produced in any standard particle interaction where fermions are created, provided the production is kinematically allowed. Consequently, the frequency of such interactions in particle collisions at typical accelerators varies significantly with the mCP mass. Figure 2 shows the different mCP production mechanisms in 13 TeV pp collisions.

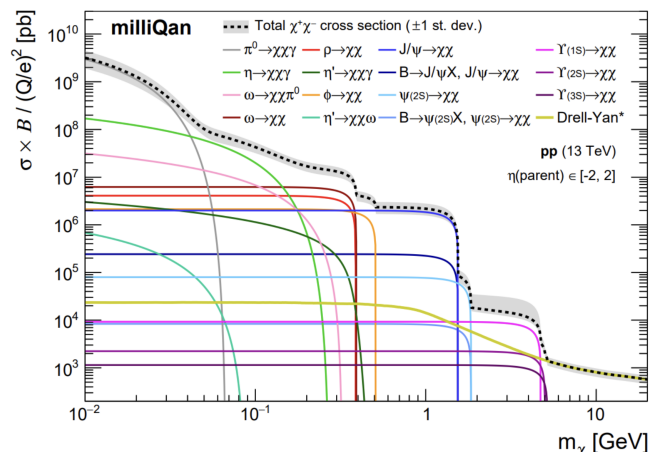


FIG. 2: Product of cross section and branching ratios as a function of the mCP (χ) mass. A description of event simulation is summarized in Ref. [21].

The primary mechanisms for millicharged particle production are QCD-inspired processes. In proton-proton collisions, significant production channels include Drell-Yan processes and decays involving η , η' , ρ , and J/ψ mesons.

II. EXPERIMENTAL OVERVIEW

Given that the energy deposited by fractionally charged particles scales with Q^2 , a particle with charge on the order of 10^{-3} has an ionisation energy loss (dE/dx) of 10^{-6} of a particle with $Q = e$. Hence, a detector designed to look for mCPs must have a large sensitive area and be able to produce small single photon signals.

While direct searches for mCPs cover many regions of the parameter space [23], the mass range $1 \text{ GeV} < m_\chi < 100 \text{ GeV}$ — which is well-suited for production at the LHC — remains largely unexplored by direct detection

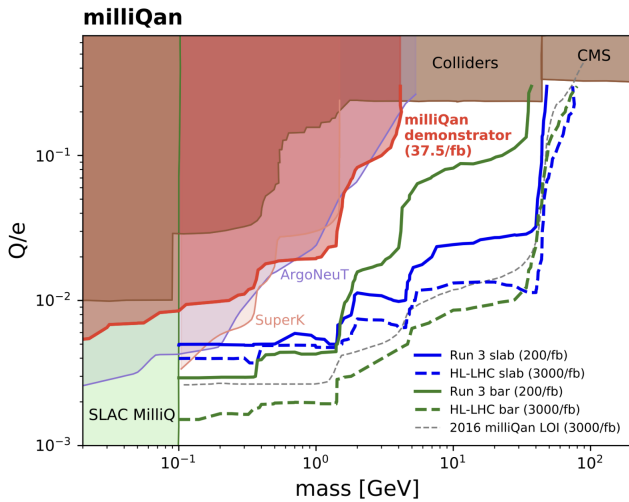


FIG. 3: Millicharged mass-charge space for milliQan demonstrator (indicated in red), Bar detector (green), and Slab detector (blue). The sensitive phase space of mass and charge of millicharged particles (mCPs) is limited by both direct searches conducted in accelerator experiments and indirect observations from various astrophysical systems [22].

efforts. The milliQan experiment specifically targets this previously unexplored phase space.

A. MilliQan Bar Detector

The milliQan bar detector is designed to target a relatively low-charge and high-mass region of the mCP phase-space (see Figure 3)[22].

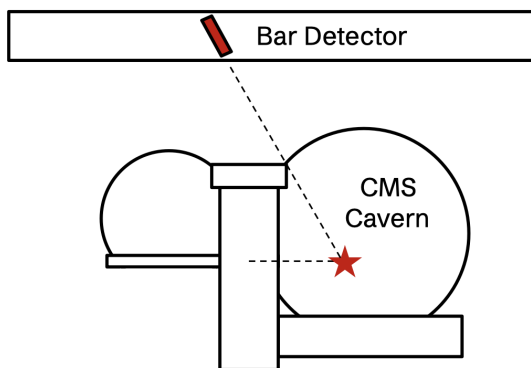


FIG. 4: milliQan Bar Detector positioned in an access tunnel 33 m away from the CMS experimental cavern.

Located at the Large Hadron Collider, the bar detector is positioned in an underground service tunnel 33 m away from the CMS interaction point (see Figure 4).

As shown in Figure 5, the detector is composed of four layers, each containing a 4×4 grid of $5 \text{ cm} \times 5 \text{ cm} \times 60 \text{ cm}$ scintillator bars with Photomultiplier Tubes (PMTs) mounted at their ends. These bars make up most of the detector and are surrounded by scintillator panels on the sides and top surface of the detector with additional panels covering the front and back of the detector. The side and top panels allow for cosmic shower vetoes and shielding from other background sources, while the front and back panels offer an additional method for tagging through-going particles.

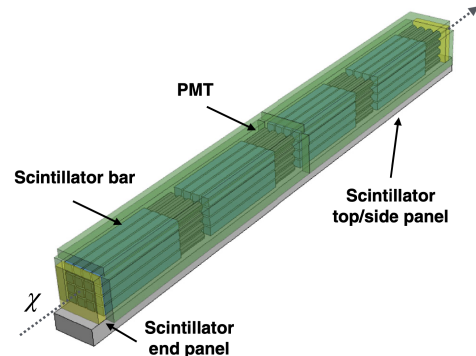


FIG. 5: Design of milliQan Run 3 Bar Detector with plastic scintillator arrays. Scintillator panels cover the top, sides, front and back of the arrays to improve efficiency and provide additional timing information [22].

When a charged particle passes through a scintillator, it emits light in the form of photons. For millicharged particles, which have a very small charge, the light produced is approximately 10,000-100,000 times fainter than that from more highly charged particles like muons. Hence, it is necessary to detect individual photons to identify these low-charge particles accurately. The detection of scintillation photons is accomplished using PMTs.

PMTs operate through a photocathode (see Figure 6) - a photosensitive surface that emits electrons when it absorbs incident photons via the photoelectric effect. These emitted photoelectrons are accelerated toward a series of dynodes designed to release secondary electrons upon impact. Each dynode is maintained at a progressively higher voltage relative to the previous one, creating an electron cascade effect. As the photoelectrons collide with successive dynodes, they release additional electrons, amplifying the initial signal. The resulting electrons are collected at the anode, generating a measurable current that is proportional to the number of photons initially detected. This current is then converted into a measurable voltage pulse as the output of the PMT. The emission of a single photoelectron (SPE) from the photocathode produces a peak in the pulse height distribution corresponding to the lowest detectable, single-photon signal.

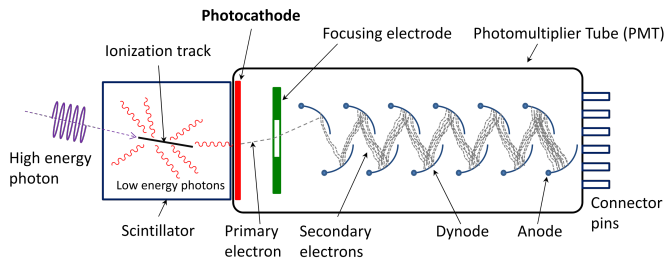


FIG. 6: A diagram of a scintillator and PMT [24]. The photocathode emits photoelectrons that then travel through the dynodes in the PMT. By the time the photoelectrons reach the anode, the single photon that initiated the process has been transformed into a large number of electrons, creating a measurable electric current. This output signal allows detection of low light levels, down to a single photon.

The bar detector’s location was carefully chosen to ensure that the majority of radiation from LHC collisions at the interaction point is absorbed by the surrounding rock before reaching the detector (see Figure 4). Despite this, some radiation still penetrates. Understanding the potential sources of background for the milliQan bar detector is crucial for accurately modeling the detector’s sensitivity. Major background sources include beam muons, cosmic muons, dark rate, and light leaks. Section III focuses on analyzing the beam muon and dark rate background in order to assess the detector’s response and confirm expected sensitivity.

B. Background

High-energy muons originating from beam collisions can penetrate the 17 meters of rock shielding and reach the detector. Despite their ability to pass through this material, these muons deposit a significant amount of energy, which makes them very unlikely to mimic a signal from a millicharged particle. Though beam muons saturate the readout, they otherwise have signal-like trajectories and are thus a useful proxy for studying millicharged particles.

Additionally, cosmic muons are produced when cosmic rays interact with the Earth’s upper atmosphere and produce pions, which further decay into muons and neutrinos. Unlike beam muons, which are expected to have a well-defined angular distribution in the detector due to alignment, cosmic muons are more challenging to detect because they have a random spatial distribution (see Figure 7). Timing calibrations and scintillator side panels are used to aid in identification.

While these muons represent a significant component of the background for milliQan, other sources of background are also considered. PMTs, crucial for detecting scintillation photons, can themselves

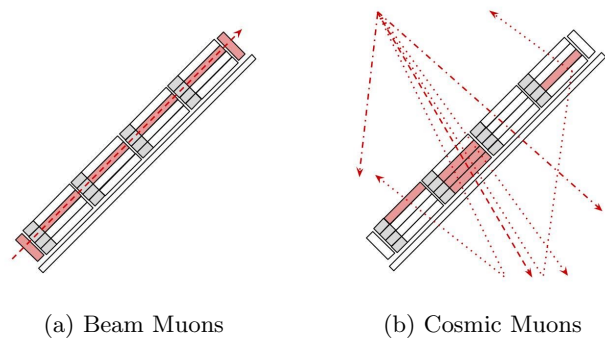


FIG. 7: Schematic view of background sources from beam and cosmic muons. Beam muons travel through all layers of the detector in the same trajectory a mCP would. Cosmic muons produce showers that cause varied responses in the detector.

contribute to background noise through dark current and electronic noise. The detector’s dark rate, the rate of spurious signals produced in the absence of actual particle interactions, adds to the challenge of distinguishing true signals from noise. In addition to these background contributions, we have also detected sub-single photoelectron (sub-SPE) responses in the PMTs (see Figure 8).

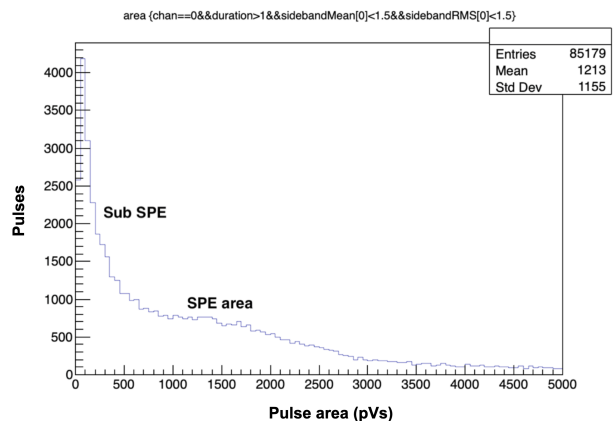


FIG. 8: Distribution of pulse area for a single channel. A prominent sub-SPE peak is observed, slightly obscuring the SPE distribution. Plot created by Matthew Citron (UC Davis).

These sub-SPE events are likely due to dynode dark rate (see Figure 9), which occurs when the dynode spontaneously emits electrons, and/or failed photoelectron detection (see Figure 10), where the photoelectron misses the first dynode. Although these events involve some level of photoelectron production, they do not represent the full amplification expected.

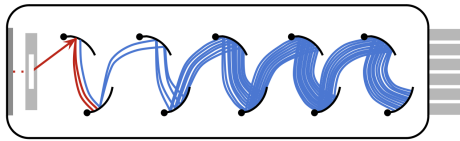


FIG. 9: The dynode dark rate refers to the rate at which dark counts occur in a PMT due to the inherent noise present in the device, specifically related to the dynode stage. Thermal and quantum effects can lead to the spontaneous emission of electrons from the photocathode or dynode, producing observable sub-SPE pulses.

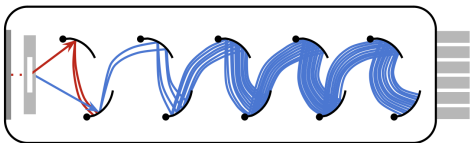


FIG. 10: A failed photoelectron refers to a situation in which an electron emitted from the photocathode of a PMT does not successfully reach the first dynode, resulting in incomplete amplification of the signal.

III. ANALYSIS

The selection of beam muons involves identifying signals that have a characteristic signature similar to millicharged particles, but with a different charge. To isolate these signals, we apply specific selection criteria to eliminate background contributions.

When PMTs detect photoelectrons, they generate pulses which are characterized by their amplitude (voltage), duration (time), and total area - the product of the voltage over time. The area under the pulse waveform, known as the pulse area, is directly linked to the number of photoelectrons detected.

Due to their relatively high energy deposits, beam muons generate saturating signals. As illustrated in Figure 11, beam muons exhibit a characteristic saturation peak in pulse area above 600,000 pVs. The less defined peak slightly below 100,000 pVs in Figure 11 is likely due to secondary cosmic muon showers as they are present in beam on and beam off runs with a comparable distribution.

Following the pulse area, we require a hit in each layer of the detector, which helps reject background signals from cosmic muon shower secondaries. Given that these cosmic muon showers can produce a spread of activity throughout the entire detector, we also implement a slope requirement to ensure that the signal aligns with a particle originating from the interaction point. These signals must arrive within a time frame consistent with the expected timing of beam muons, which from previous studies has been determined to be 15 ns [22]. This

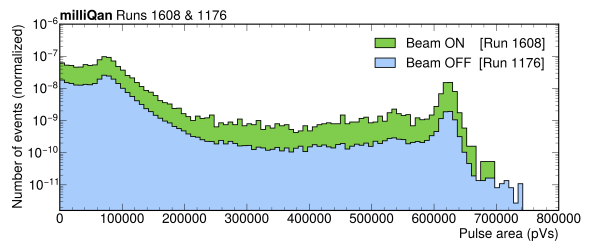


FIG. 11: Pulse area of a beam on and beam off run with no cuts applied. Saturation occurs slightly above 600,000 pVs in both runs.

narrow timing window helps to veto backgrounds like overlapping dark rate pulses which are uncorrelated in time. The full list of selection cuts applied to the data is detailed in Table I.

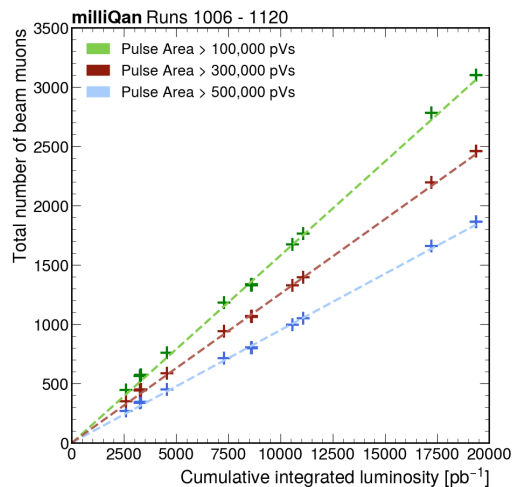


FIG. 12: Total number of beam muons as a function of integrated luminosity.

Identified beam muons are then compared with integrated luminosity in Figure 12. We observe a linear correlation between integrated luminosity and the number of beam muons, with fewer events passing the beam muon selection cuts as the pulse area threshold increases. Once a slope requirement is applied to 12, the beam muon rates for area thresholds of 300,000 pVs and 500,000 pVs show no substantial difference, whereas the 100,000 pVs threshold yields significantly fewer passing events. With more hits passing the beam muon selection at lower area thresholds, the likelihood of reconstructing the track as a zero-slope path directly through the detector decreases. A threshold of 300,000 pVs in pulse area offers a clear identification of beam muons while remaining sufficiently inclusive, making it suitable for future beam muon identification studies.

Although beam muons play a significant role in assessing the detector's response, performance, and alignment, the real challenge lies in understanding how the detector responds to SPE deposits. This is critical

TABLE I: Beam muon signal selection and characterization as a result of the study

Selection	Criterion
Pulse area threshold	pulse area $\geq 300,000$ pVs
Timing	$ \Delta t \geq 15$ ns
Layers hit	4 layers
Slope requirement	straight path

because a mCP signal is on the order of single photons, which makes it important to accurately characterize the detector's response at such low signal levels. To illustrate this, Figure 8 presents a plot of the sub-SPE distribution, showing signals below the typical SPE range. Sub-SPE signals refer to charge deposits that are smaller than a single photoelectron. These can occur due to dynode dark rate and failed photoelectron trajectories, but can be challenging to distinguish from true SPE events.

Understanding and properly modeling this sub-SPE response is crucial to reducing background and improving the sensitivity of the detector to mCP-like signals. Motivated by the observation of sub-SPE pulses in milliQan data, we examined the sub-SPE excess present in PMTs in the lab with the setup shown in Figure 13. In this configuration, four PMTs were mounted to the sides of a rectangular scintillator slab (see Figure 13). A series of light-emitting diodes (LEDs) was arranged at one end of the slab (refer to Figure 14). Each PMT was powered by a common high-voltage supply, and a function generator was used to control both the trigger signals and the LED pulses. A Domino Ring Sampler (DRS) was used for configuring the channels and trigger logic and reading out the digitized PMT waveforms [25].

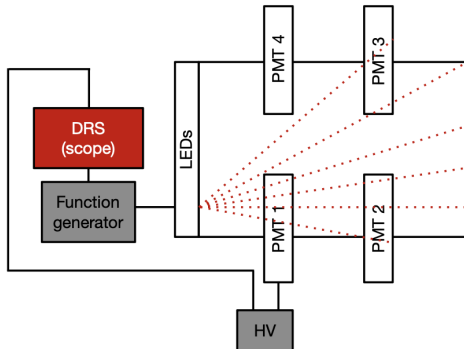


FIG. 13: Lab PMT setup. Four bars containing plastic scintillators and high-gain PMTs, each with a different quantum efficiency, are mounted against the edge of the slab.

To validate hypotheses concerning the dynode dark rate and the trajectories of failed photoelectrons, we employed a series of LED flashes to induce changes in the SPE and sub-SPE distributions. LEDs were used in

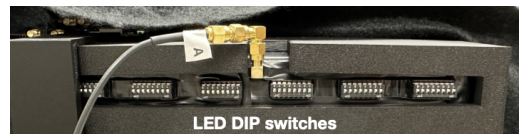


FIG. 14: The LEDs in the laboratory setup are controlled by dip switches. Each switch, when toggled, either completes or breaks circuits on a circuit board, sending signals to the connected components.

the experimental setup to generate more photoelectrons at the photocathode, which aids in distinguishing between photoelectrons produced by the LEDs and those generated within the dynodes (which may be affected by factors such as the dynode dark rate). By systematically varying the LED flash intensity, we were able to generate a range of light levels and signal variations in the PMTs.

As observed in Figure 15, the SPE peak increases with higher number of LEDs flashed while the sub-SPE maintains the same shape. These results indicate that the sub-SPE excess is likely due to dynode dark rate as it remains constant regardless of the number of LEDs flashed. If the failed photoelectron effect were the contributing factor, the observed sub-SPE peak would change with the number of LEDs.

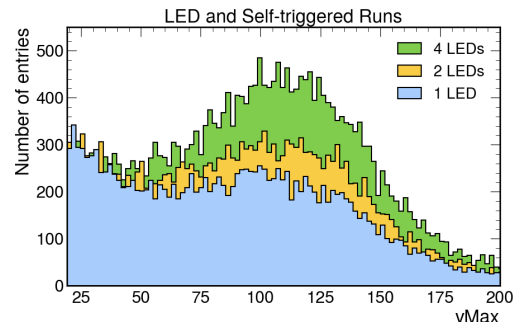


FIG. 15: Distribution of vMax (largest absolute value voltage in the event) as a function of the number of LEDs switched on. The sub-SPE distribution remains the same regardless of the number of LEDs turned on.

Given that dynode dark rate is caused by a thermionic emission of photoelectrons, we also expect the sub-SPE excess to decrease with decreasing temperature. Several tests were carried out to investigate temperature effects, using external cooling or heating of the PMT. Challenges emerged with these configurations, as the internal temperature of the PMTs did not align with readings from temperature sensors; thus, additional studies should be conducted to understand dark rate's temperature dependence. Once sub-SPE pulses are accurately modeled, these contributions can be subtracted from the data, thereby isolating the SPE distribution and optimizing sensitivity to mCPs.

IV. SUMMARY AND OUTLOOK

Millicharged particles are supported by various theoretical models and their discovery could have significant implications for our understanding of charge quantization and the exploration of the dark sector. The milliQan detector is uniquely equipped to probe these particles with its exceptional sensitivity. Our analysis has validated selection criteria for tagging beam muons. To build on this progress, future efforts will focus on investigating cosmic muons, refining simulation models, and further explorations of dark rate and PMT performance. A new bar has also been constructed this summer with three different PMTs (R878, H3178-51, and H11901), which will allow more detailed studies of pulse timings as well as tests of different LEDs.

ACKNOWLEDGMENTS

I would like to thank Prof. David Stuart for his invaluable guidance and support throughout this research. I am deeply grateful for being welcomed into the lab and for the opportunity to learn and develop both analysis and hardware skills. I also owe a great deal of thanks to Ryan Schmitz and Neha Santpur, for teaching me the theoretical principles and for dedicating time to assist with questions and provide valuable feedback. Thank you all for your guidance, encouragement, and for making this summer a memorable and fulfilling experience. My sincere appreciation goes to the entire milliQan collaboration. I would also like to thank Prof. Sathya Guruswamy, the UCSB Physics REU Site Director, for making this opportunity possible and greatly engaging. This work was supported by NSF REU Grant PHY-2349677.

-
- [1] CERN, The Standard Model (2023).
 - [2] X. Fan, T. G. Myers, B. A. D. Sukra, and G. Gabrielse, Measurement of the electron magnetic moment, *Phys. Rev. Lett.* **130**, 071801 (2023).
 - [3] Y. Fukuda *et al.* (Super-Kamiokande Collaboration), Evidence for oscillation of atmospheric neutrinos, *Phys. Rev. Lett.* **81**, 1562 (1998).
 - [4] F. Zwicky, Republication of: The redshift of extragalactic nebulae, *General Relativity and Gravitation* **41**, 207 (2009).
 - [5] J. Silk *et al.*, *Particle Dark Matter: Observations, Models and Searches*, edited by G. Bertone (Cambridge Univ. Press, Cambridge, 2010).
 - [6] D. Akerib *et al.*, Limits on spin-dependent wimp-nucleon cross section obtained from the complete lux exposure, *Physical Review Letters* **118**, 10.1103/physrevlett.118.251302 (2017).
 - [7] E. Aprile *et al.*, Dark matter search results from a one ton-year exposure of xenon1t, *Physical Review Letters* **121**, 10.1103/physrevlett.121.111302 (2018).
 - [8] M. Kamionkowski, Wimp and axion dark matter (1997), arXiv:hep-ph/9710467 [hep-ph].
 - [9] S. Gori, M. Williams, P. Ilten, N. Tran, G. Krnjaic, N. Toro, B. Batell, N. Blinov, C. Hearty, R. McGehee, P. Harris, P. Schuster, and J. Zupan, Dark sector physics at high-intensity experiments (2022), arXiv:2209.04671 [hep-ph].
 - [10] C. Collaboration, Dark sector searches with the cms experiment (2024), arXiv:2405.13778 [hep-ex].
 - [11] B. Holdom, Two $u(1)$'s and charge shifts, *Physics Letters B* **166**, 196–198 (1986).
 - [12] P. Langacker and S.-Y. Pi, Magnetic monopoles in grand unified theories, *Phys. Rev. Lett.* **45**, 1 (1980).
 - [13] A. A. Prinz, R. Baggs, J. Ballam, S. Ecklund, C. Fertig, J. A. Jaros, K. Kase, A. Kulikov, W. G. J. Langeveld, R. Leonard, T. Marvin, T. Nakashima, W. R. Nelson, A. Odian, M. Pertsova, G. Putallaz, and A. Weinstein, Search for millicharged particles at slac, *Phys. Rev. Lett.* **81**, 1175 (1998).
 - [14] G. Magill, R. Plestid, M. Pospelov, and Y.-D. Tsai, Millicharged particles in neutrino experiments, *Phys. Rev. Lett.* **122**, 071801 (2019).
 - [15] S. Chatrchyan and Anonymous (CMS Collaboration), Erratum: Search for fractionally charged particles in pp collisions at $\sqrt{s} = 7$ TeV [phys. rev. d 87, 092008 (2013)], *Phys. Rev. D* **106**, 099903 (2022).
 - [16] S. Chatrchyan *et al.*, Searches for long-lived charged particles in pp collisions at $\sqrt{s} = 7$ and 8 tev, *Journal of High Energy Physics* **2013**, 10.1007/jhep07(2013)122 (2013).
 - [17] L. B. Auerbach *et al.* (LSND Collaboration), Measurement of electron-neutrino electron elastic scattering, *Phys. Rev. D* **63**, 112001 (2001).
 - [18] Aguilar-Arevalo *et al.* (The MiniBooNE-DM Collaboration), Dark matter search in nucleon, pion, and electron channels from a proton beam dump with miniboone, *Phys. Rev. D* **98**, 112004 (2018).
 - [19] R. Acciarri *et al.* (ArgoNeuT Collaboration), Improved limits on millicharged particles using the argoneut experiment at fermilab, *Phys. Rev. Lett.* **124**, 131801 (2020).
 - [20] L. Barak *et al.*, Sensei: Search for millicharged particles produced in the numi beam (2023), arXiv:2305.04964 [hep-ex].
 - [21] A. Ball *et al.*, Search for millicharged particles in proton-proton collisions at $\sqrt{s} = 13$ TeV, *Phys. Rev. D* **102**, 032002 (2020).
 - [22] A. Ball, J. Brooke, C. Campagnari, M. Carrigan, M. Citron, A. De Roeck, M. Ezeldine, B. Francis, M. Gastal, M. Ghimire, *et al.*, Sensitivity to millicharged particles in future proton-proton collisions at the lhc with the milliQan detector, *Physical Review D* **104**, 10.1103/physrevd.104.032002 (2021).
 - [23] S. Davidson, S. Hannestad, and G. Raffelt, Updated bounds on milli-charged particles, *Journal of High Energy Physics* **2000**, 003 (2000).
 - [24] W. Commons, Schematic view of a photomultiplier coupled to a scintillator,

- illustrating detection of gamma rays (2013), file: PhotoMultiplierTubeAndScintillator.svg.
- [25] S. Ritt, R. Dinapoli, and U. Hartmann, Application of the drs chip for fast waveform digitizing, *Nuclear Instruments and Methods in Physics Research Section A: Accelerators, Spectrometers, Detectors and Associated Equipment* **623**, 486 (2010), 1st International Conference on Technology and Instrumentation in Particle Physics.
- [26] M. D. Citron, Search for millicharged particles at the lhc with the milliqa prototype, *Proceedings of 40th International Conference on High Energy physics — PoS(ICHEP2020) 10.22323/1.390.0232* (2021).
- [27] A. Haas, C. S. Hill, E. Izaguirre, and I. Yavin, Looking for milli-charged particles with a new experiment at the lhc, *Physics Letters B* **746**, 117–120 (2015).
- [28] H. Zaraket, The milliqa experiment: Search for milli-charged particles at the lhc, *Proceedings of European Physical Society Conference on High Energy Physics — PoS(EPS-HEP2019) 10.22323/1.364.0578* (2020).
- [29] E. Izaguirre and I. Yavin, New window to millicharged particles at the lhc, *Phys. Rev. D* **92**, 035014 (2015).